Icarus 222 (2013) 550–558

Contents lists available at SciVerse ScienceDirect

Icarus

journal homepage: www.elsevier.com/locate/icarus

Shape, density, and geology of the nucleus of Comet 103P/Hartley 2

P.C. Thomas [a,*], Michael F. A'Hearn [b], Joseph Veverka [a], Michael J.S. Belton [c], Jochen Kissel [d], Kenneth P. Klaasen [e], Lucy A. McFadden [b,f], H. Jay Melosh [g], Peter H. Schultz [h], Sébastien Besse [b], Brian T. Carcich [a], Tony L. Farnham [b], Olivier Groussin [i], Brendan Hermalyn [h], Jian-Yang Li [b], Don J. Lindler [j], Carey M. Lisse [k], Karen Meech [l], James E. Richardson [g]

[a] Center for Radiophysics and Space Research, Cornell University, Ithaca, NY 14853, USA
[b] Department of Astronomy, University of Maryland, College Park, MD 20742-2421, USA
[c] Belton Space Exploration Initiatives, LLC, 430 S. Randolph Way, Tucson, AZ 85716, USA
[d] Max Planck Institute for Solar System Research, Katlenburg-Lindau, Germany
[e] Jet Propulsion Laboratory, California Institute of Technology, 4800 Oak Grove Drive, Pasadena, CA 91109, USA
[f] NASA Goddard Space Flight Center, Greenbelt, MD 20771, USA
[g] Purdue University, Lafayette, IN 47907, USA
[h] Department of Geological Sciences, Brown University, Providence, RI 02912, USA
[i] Laboratoire d'Astrophysique de Marseille, Université de Provence and CNRS, Marseille, France
[j] Sigma Space Corp., 4600 Forbes Blvd., Lanham, MD 20706, USA
[k] JHU-Applied Physics Laboratory, 11100 Johns Hopkins Rd., Laurel, MD 20723, USA
[l] Institute for Astronomy, University of Hawaii, 2680 Woodlawn Dr., Honolulu, HI 96822, USA

ARTICLE INFO

Article history:
Available online 7 June 2012

Keywords:
Comets
Comets, Nucleus
Geological processes
Geophysics

ABSTRACT

Data from the Extrasolar Planet Observation and Deep Impact Extended Investigation (EPOXI) mission show Comet 103P/Hartley 2 is a bi-lobed, elongated, nearly axially symmetric comet 2.33 km in length. Surface features are primarily small mounds <40 m across, irregularly-shaped smooth areas on the two lobes, and a smooth but variegated region forming a "waist" between the two lobes. Assuming parts of the comet body approach the shape of an equipotential surface, the mean density of Hartley 2 is modeled to be 200–400 kg m^{-3}. Such a mean density suggests mass loss per orbit of >1%. The shape may be the evolutionary product of insolation, sublimation, and temporary deposition of materials controlled by the object's complex rotation.

1. Introduction

After carrying out an impact experiment on Comet 9P/Tempel 1 (A'Hearn et al., 2005a) the Deep Impact mission's flyby spacecraft was retargeted to Comet 103P/Hartley 2 as part of an extended mission named EPOXI. Compared to Deep Impact's first target, Hartley 2's nucleus is one-fifth the size yet produces a similar amount of outgassing at perihelion (Groussin et al., 2004; Lisse et al., 2009; Meech et al., 2011). This high level of activity made 103P/Hartley 2 an especially interesting target, and for expectations that its surface features would differ from those of Tempel 1.

Closest approach to Hartley 2 was 694 km at 13:59:47.31 UTC on 4 November 2010, 1 week after perihelion passage and 1.064 AU from the Sun. The images confirmed that its surface is very different from that of Tempel 1, and indeed from the other comets so far visited by spacecraft (A'Hearn et al., 2011; Schultz et al., 2011).

We use the image data to produce a shape model (refined from that reported in A'Hearn et al. (2011)) and surface feature maps. These products are then used to investigate the processes effective at the comet's surface, its mean density, and some aspects of its evolution.

2. Data and methods

Because the Hartley 2 encounter has been described in depth in A'Hearn et al. (2011), we summarize only the most pertinent imaging instrumental details here. The Deep Impact spacecraft and its instruments are described in A'Hearn et al. (2005b), Hampton et al. (2005), and Klaasen et al. (2008). Most of the work reported here has used the EPOXI Medium Resolution Instrument (MRI) camera data; these have a pixel scale of ~7 m at the closest approach of 694 km. The EPOXI High Resolution Instrument (HRI) nominally produces images at ~5 times better resolution than MRI, but was found to be out of focus after launch (Klaasen et al., 2008). Deconvolution (Lindler et al., 2012) can render some of these images suitable for studying forms smaller than are visible

* Corresponding author.
E-mail address: pct2@cornell.edu (P.C. Thomas).

0019-1035/$ - see front matter © 2012 Elsevier Inc. All rights reserved.
http://dx.doi.org/10.1016/j.icarus.2012.05.034

Table 1
Characteristics of Hartley 2.

Area: 5.24 km^2
Volume: 0.809 ± 0.077 km^3
Mean radius: 0.58 ± 0.018 km
Diameter range: 0.69–2.33 km
Gravity: 0.0019–0.0044 cm s^{-2} (if mean density = 300 kg m^{-3})
Model moments: 5.302×10^4, 31.26×10^4, 31.92×10^4 m^2
Model moment ratios: A/C: 0.166 ± 0.004, B/C: 0.979 ± 0.002
Body model moment orientations: A: 89.73°, 207.56°E; B: 0.05°, 106.14°E; C: 0.25°, 16.14°E
Long axis at closest approach: RA: 226.12°, Dec: 39.37° 2010–2011-04T13:59:47.7
Minimum moment at closest approach: RA: 225.92 ± 0.9°, Dec: 39.60 ± 0.7°
Intermediate moment at closest approach: RA: 330.0, Dec: 16.3, ±12° along arc perpendicular to minimum moment

in the MRI data, but this processing often introduces artifacts that complicate their use in geological interpretation.

Most useful MRI data were obtained within a range of 1600 km of the comet (16 m/pixel) and span phase angles of 80–94°. A few HRI images were useful out to ranges of ~2500 km. Navigation data in the form of "SPICE" kernels (Semenov et al., 2004; Semenov and Acton, 2006) are the basis for all geometric work on the comet. An important characteristic of this comet is its complex rotation (Belton et al., 2012) which limits any mapping convention that would be tied to the surface. This rotation includes a primary period, increasing through encounter, and a roll about the long axis, with a decreasing period. Most useful mapping data were obtained within a period when a simplified model of rotation predicts that the object orientation changes by ~0.6°. Because of our desired mapping conventions (see below), the routine mapping was done with a simple rotation model that is likely to introduce relative position errors of 0.3° between extremities of the object. This error is less than 1 pixel at the ends of the object.

Determination of the shape and accurate relative positioning of the images relies upon stereo control points with image pointing adjustments (Thomas et al., 2002). There are 244 manually measured points in the ~50% of the comet that is directly observed. Good control of much of the rest of the shape is provided by pronounced nightside silhouettes arising from light scattered from the coma. The mean control point residuals of 0.29 pixel, or ~3 m suggest that mean dimensions of the comet for the ~50% constrained by the stereo data are good to ±10 m. Much of the rest of the surface determined from silhouettes is good to ±30 m; most of the uncertainty arises from the ambiguity of where a limb pixel is along the line of sight. Combining the areas and uncertainties, we estimate the mean radius (radius of sphere of equivalent volume) is measured to 18 m accuracy (1 sigma); see Table 1.

Mapping of features and projection of images uses image cubes that store latitude, longitude, radius, incidence, and emission at each pixel. Line and sample coordinates of features marked in the images or the image data themselves can then be arbitrarily projected.

Quantities such as gravity and slope are calculated with an assumed mean density and rotation vectors. We discuss the determination of the nucleus' mean density in detail in Section 5. "Topography" is calculated as dynamic height, the surface potential energy divided by an average acceleration (Vanicek and Krakiwsky, 1986; Thomas, 1993) which is close to the height above a reference equipotential. The dynamic heights also depend upon mean density and rotation rate and are studied in Section 5.

Mapping uses a prominent feature as a prime meridian: a dark spot, actually including part of a shaded side and shadow cast from a 20-m high mound. The map coordinate system used here is oriented on the basis of the bi-lobed shape: the long axis is taken to be the latitude direction. Given the complex and changing rotation (Belton et al., 2012) latitudes and longitudes cannot be tied to any rotation element. Our maps are not intended as IAU proposals.

The cylindrical mapping of such an elongate, bi-lobate object has distorted areas no matter the orientation. Here we use both simple cylindrical and a pseudo-equal area projection to better handle high latitude data. This method simply measures the distance along latitude lines from a reference longitude, and scales the north–south coordinate to the average length of a longitude line. This scheme is particularly suited to a nearly axially-symmetric object such as Hartley 2 because the length of the longitude lines varies only slightly.

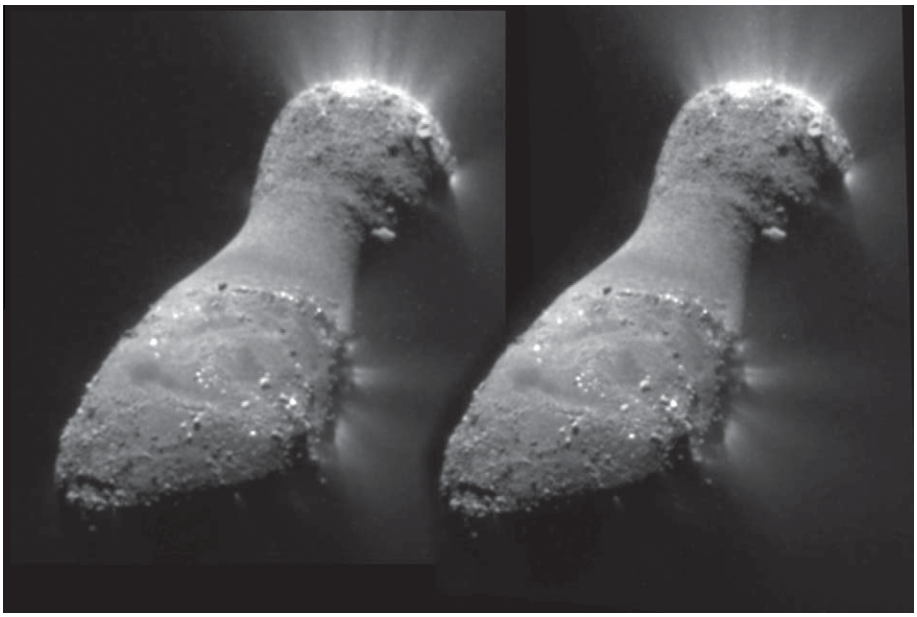

Fig. 1. Stereo view of Hartley 2. Images are mv0342149303_6000002 and mv0342149307_5004051 obtained from ranges of 695 and 697 km. Smaller lobe is the northern one; Sun is from slightly left of up. Right side is the evening terminator. Zero longitude goes through the dark spot (partly a shadow) mid way up the body, close to the limb at the left side.

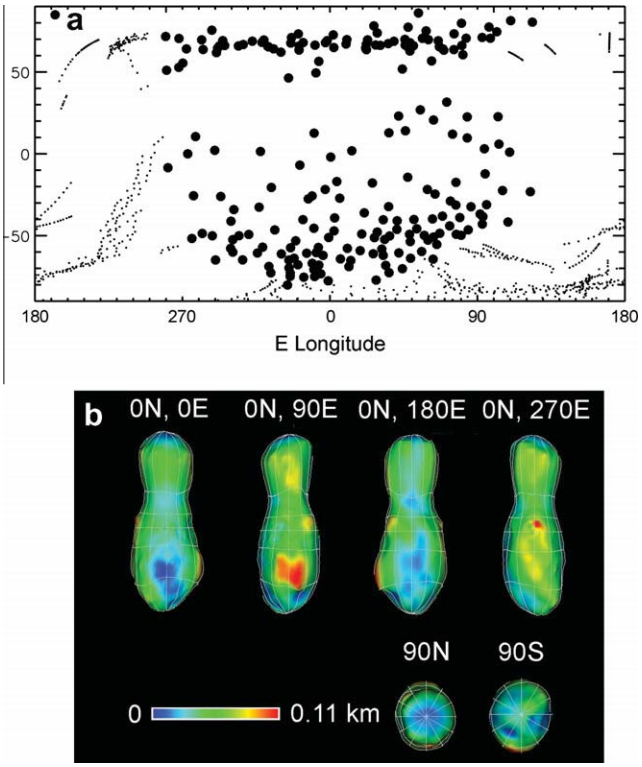

Fig. 2. Shape data and shape. (a) Limb and control point data locations, simple cylindrical projection. Large dots are control point solutions, small dots are calculated limb and silhouette positions. (b) Shape model colored by relative dynamic heights. (For interpretation of the references to color in this figure legend, the reader is referred to the web version of this article.)

3. Overall results

Global characteristics of Hartley 2 are listed in Table 1. Preliminary values, close to these, were presented in A'Hearn et al. (2011); updates to the shape have largely been local changes of <20 m from addition of control points and more limb control. Fig. 1 presents a stereo view at the best MRI resolution which covers most of the visible object. Fig. 2 shows coverage for data that control the calculation of the shape, as well as views of the resulting shape model shaded by the dynamic heights. The mean radius (radius of a sphere of equivalent volume) of 0.580 ± 0.018 km found here is indistinguishable from that calculated before encounter by Lisse et al. (2009) using Spitzer data to determine the effective radius of the cross-section at the time of observation. This bi-lobed object has near rotational symmetry: calculated moments, assuming a homogeneous interior, have relative values of 1.000, 0.979 ± 0.002, 0.166 ± 0.004. These model moment ratios are unusually but not uniquely symmetric. For comparison, the model moment ratio B/C for Tempel 1 is 0.931, it is 0.982 for asteroid Eros, and it is 0.980 for satellite Epimetheus. Several other Saturnian small satellites' B/C range from 0.819 to 0.886 (These values calculated by PT). That Hartley 2 is not exactly symmetric is noticeable in Fig. 1 when carefully viewing the larger lobe. Nonetheless, this object does not have the asymmetries that are seen on many impact-shaped objects (Thomas, 1989). Note that an object such as Eros can have moment ratios of nearly 1 while having a distinctly banana-like shape.

4. Terrain types and surface features

The surface of Hartley 2 is approximately divisible into two rough lobes connected by a smooth "waist" (Figs. 1 and 2). Surface

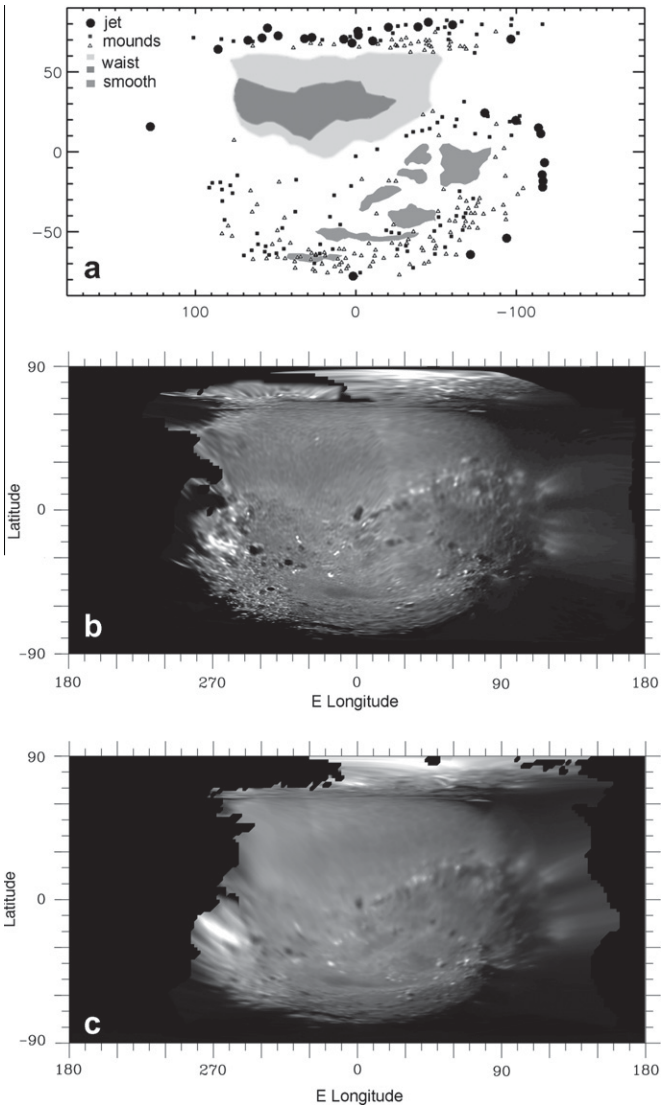

Fig. 3. Cylindrical projection maps. (a) Mapped features. Note that there are separate bright and dark mound symbols; these are qualitative classifications only. Darker and lighter portions of the waist are differentiated. Other smooth areas are mapped separately. (b) HRI image mosaic. (c) MRI images.

maps are shown in Figs. 3 and 4. In detail the surface combines varying distributions of mounds generally less than 30 m in any dimension, and substantially smoother terrain (at 7 m/pixel). While the latitudinally confined waist is the largest smooth area, other smooth areas of irregular outline occur in parts of the larger lobe.

4.1. Mounds

The roughness of Hartley 2 derives from the presence of mounds, mostly only a few pixels across, and most of which are crudely equidimensional. However, a few of these are unusually elongated, either nearly normal to the surface or at low angles to the surface (Fig. 1). There are a few spires greater than 40 m in height, one of which appears in stereo viewing to be angular in shape with a probable overhang (upper part of Fig. 1 near terminator). Views such as Fig. 1 suggest there are albedo differences among the mounds, but estimating reliable albedos from marginally resolved features with a variety of photometric geometries demands extreme caution. The qualitative mapping did divide

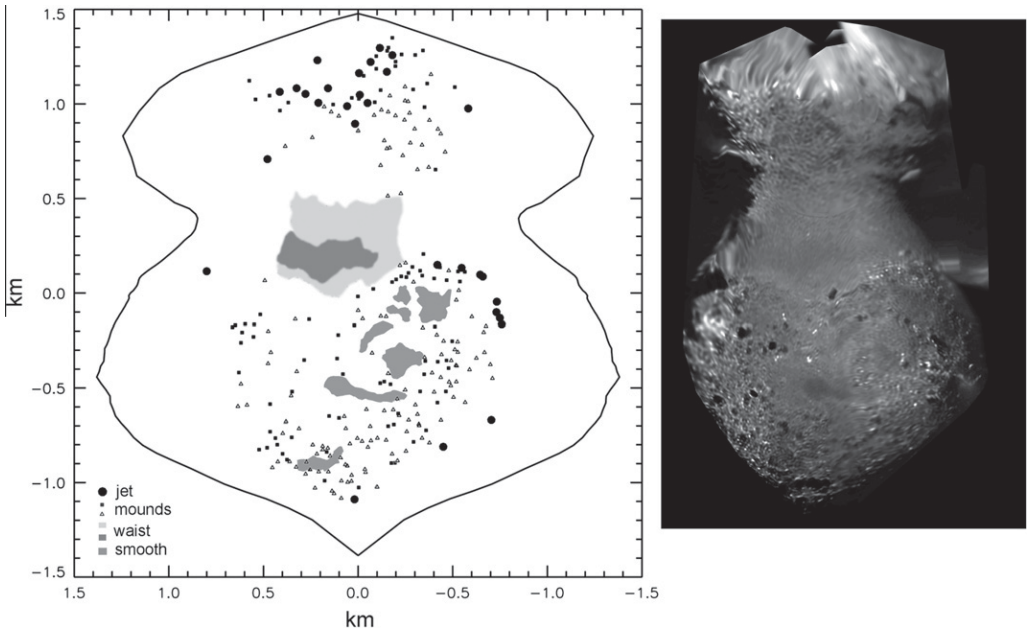

Fig. 4. Pseudo equal-area projections of Hartley 2. Left: Mapped features, same scheme as Fig. 3. Right: Image map, combining both HRI and MRI data.

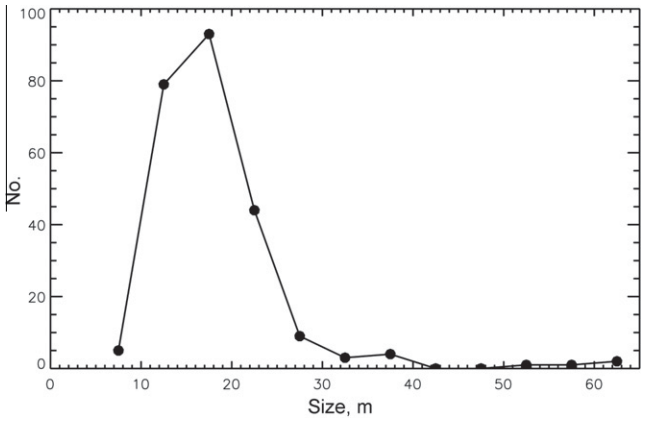

Fig. 5. Histogram of mound sizes. Data are mean horizontal dimensions; 5 m bin sizes. Fall-off below 20 m is probably largely resolution-related.

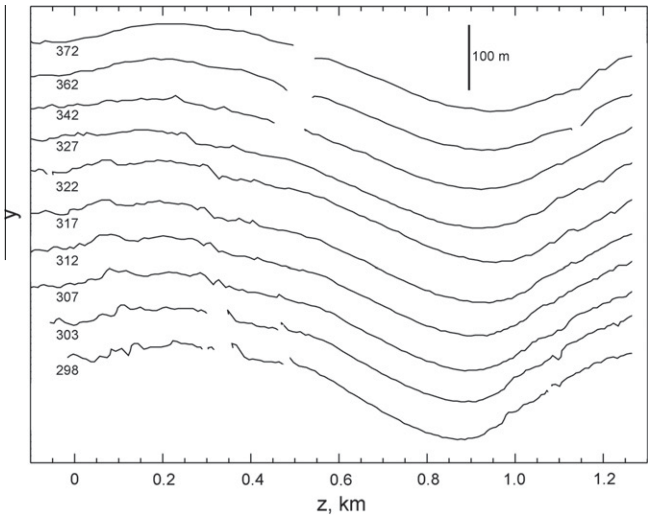

Fig. 6. Limb scans around the waist. Abscissa is the distance parallel to projection of *z* axis in the image; ordinate is limb position relative to *z* axis in image, each is offset to show relative topography. Three digit numbers are last digits of the mission elapsed time portion of MRI image numbers (for example: mv0342149372). Vertical dimension exaggerated by 1.6.

mounds by apparent relative brightness (Fig. 3), though for most purposes one should lump them together as one population of features. The size distribution of mounds (Fig. 5) suggests a large population smaller than the available resolution.

4.2. The waist

The distinctive waist (Figs. 1 and 6) is visible in images between longitudes 90–280°E and latitudes 2°S–22°N to ~60°N. Silhouettes in both HRI and MRI data show this shape occurs over nearly the full circumference of the object (Fig. 6). The surface is variegated at horizontal scales of 15–30 m. The markings in the waist, mostly only 2–3 pixels across, are repeatable image-to-image and are well-defined in stereo pairs (Fig. 7a). Thus these subtle forms are real and not simply noise. Patterns of different albedo also exist on the 100–200 m scale and suggest digitate outlines (Fig. 7a), especially near the margins. A darker region between ~10 and 40°N occupies most of the visible longitude range but fades at about 70°E. This limitation may reflect an incidence angle effect at values >60°.

The smoothness of the waist may be important in questions of its formation mechanism. Fig. 6 shows limb profiles measured to ~0.15 pixels precision (~1 m in the best images) by software specifically designed for edge detection (Dermott and Thomas, 1988). Repeatable deviations of ~2 m occur within these profiles. As with any limb profile the observed edge is a skyline smoother than a straight topographic profile over the position of the limb. Most deviations are under 1 m. The very high incidence angle region near the east end of the waist is limited in the applicability of shadows to measuring topography because some of this area is shadowed by protuberances that are part of the small lobe. The solar direction does have a westward component near the terminator, so some of the waist is seen at incidence angles above 86°. Irregularities in the terminator of ~10–15 m suggest topography of at

least ~1 m in height in this region. Thus, while the waist is smoother than the rest of the object, formative processes must cause, expose, or preserve topography of up to 2 m in height (and possibly more) on local scales up to 30 m in horizontal extent.

4.3. Other smooth areas

The large lobe has several (7 or more) irregularly-shaped areas of smoother and slightly darker appearance than the average surface of Hartley 2 (Figs. 2 and 7b). These darker areas are flanked by slightly brighter materials of varying extent. In combination with the mounds these areas comprise a sequence from the center outward of dark smooth material, brighter smooth areas, and mound–dense regions. The stereo pairs (Fig. 7b) show that these dark smooth regions range from elongate and irregular, to almost regular polygons. With strong contrast enhancement they show mottling on roughly the same horizontal scale of 15–30 m as seen in the waist, although they are less prominent than those markings within the waist.

4.4. Jets

Jets made visible by entrained dust and ice particles are prominent features of the region near the nucleus. Although the jets are not surface features, the approximate base locations are plotted in Fig. 3. These were mapped by interactive stereo viewing and plotting results on the projected shape model in single views of the surface. Because the contrasts of the jets change with viewing, and the background in most areas under the jets is variegated and rough, these positions, and even the number of jets, is subject to some interpretation. The basic occurrence pattern is reliable, and shows the association of jets with the rougher areas and mounds, and their avoidance of the smooth areas, as noted by A'Hearn et al. (2011) and Syal et al. (2012). Accurate measurement of their dimensions is beyond this work, but most are 3–5 pixels wide in the 7-m/pixel data. Detailed modeling of possible jet formation and relation to general surface evolution is reported in Syal et al. (2012).

4.5. Other patterns and forms

On the larger lobe, the region from ~260–320°E to ~20–70°N has somewhat rougher mound topography, more small spire-like mounds, and displays a somewhat higher albedo and bluer colors (Li et al., 2012) than the middle part of this lobe. The color differences appear to arise from a greater exposure of water ice (Sunshine et al., 2011; Li et al., 2012) and might relate to this area being near the morning terminator, the morphologic differences would not arise diurnally. In fact, there is a smaller region of somewhat similar increased roughness in the region 30–80°E. Thus, although topographic type varies crudely along the long axis of this object, considerable variation exists longitudinally.

5. Inferring a mean density

5.1. Inferences from averaged quantities

The distinctive, smooth profile of the waist was used by A'Hearn et al. (2011) and Richardson and Bowling (2012) to infer a mean density range for Hartley 2 using some assumptions. First, the smooth form was assumed to be at or close to an equipotential, presumably the result of depositional filling and smoothing a low area. Second, a simple 18-h rotation period was assumed about the maximum moment direction at the time of encounter. Third, the interior was assumed to be homogeneous in density. Minimizing the variation of fractional potential energy over the area of the well-imaged waist suggested a mean density of 220 kg m^{-3} (A'Hearn et al., 2011) and 140–520 kg m^{-3} (Richardson and Bowling, 2012). Here we use the updated shape model, slightly different definitions of the waist area, and considerations of whether complications in the spin have practical effects to interpret the mean density.

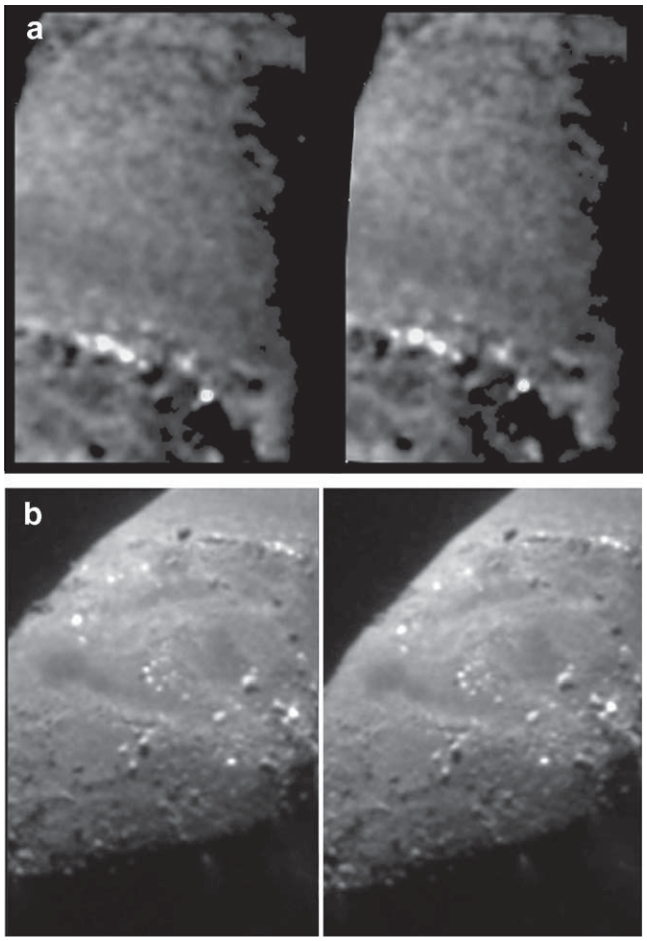

Fig. 7. Stereo views of parts of surface of Hartley 2. (a) Detail of the waist, contrast stretched to emphasize the variegated surface. North is to upper right, center is at approximately 55°N, 30°E. Panel width 430 m. Images mv342149303_6000002 and mv342149307_5004051. (b) Region with darker, smoother areas and areas of small, brighter mounds on the larger, southern lobe. North is to upper right, centered at approximately 53°S, 31°E. Panel width 810 m. Images mv342149303_6000002 and mv342149312_5004052.

The most important additional concern is the comet's complex and changing rotation (A'Hearn et al., 2011; Belton et al., 2012). First, the primary period was rapidly increasing at the time of encounter, approximately 0.1% per period; where the period was ~16 h only 60 days before encounter (Meech et al., 2011; Belton et al., 2012). Surface features are unlikely to evolve at meters/day (see Section 6.1), and thus the shape we measure and attempt to model would have formed over a considerable interval of time before the flyby. Thus, the applicable primary period would be 16 h or possibly even less. Additionally, the complex spin imposes a roll about the long axis, which for our purposes may be thought of as having two effects: (1) The primary spin pole moves; in our mapping the spin pole would move through different longitudes, varying the rotational accelerations added to the gravitational accelerations. (2) The roll slightly reduces the relative gravitational topography along the longitude lines (along the cross profiles of the waist): For a 27.8 h roll period relative topography from the middle of the waist (latitude 40°N) to the northern edge (60°N) de-

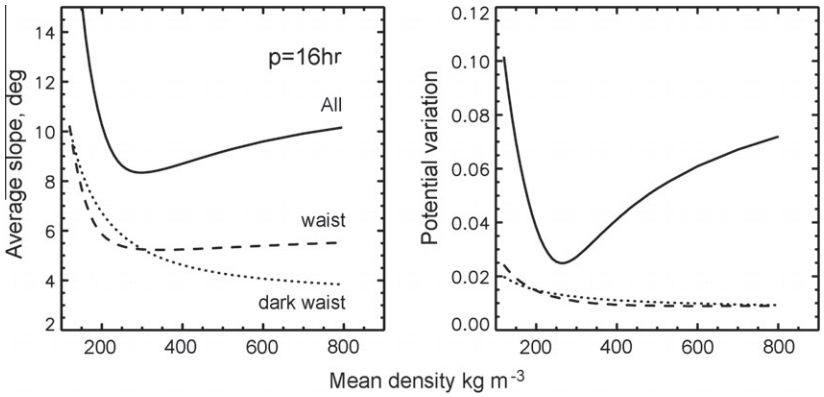

Fig. 8. Variation of slope and potential as a function of mean density. Left: Average slope, degrees, as a function of mean density for the whole object, the entire waist (see Fig. 2), and the darker portion of the waist (Fig. 2). Right: variation of potential energy for same areas as in (a).

creases by 1 m relative to a no-roll situation. Moving the spin pole position has some effect on the relative heights of points within the waist relative to the south pole because the waist is not perfectly circular along latitude lines (typically 25–30 m difference in radius from 60°E to 300°E along latitude lines in the waist). The north–south difference in dynamic heights along a particular longitude line varies by less than 1 m with the change in spin pole location. Thus, we can make comparisons based on a nominal spin pole location as the effects of the roll are effectively much smaller than is our ability to discriminate topography. We make these comparisons of heights for different densities and spin rates.

For each mean density we calculate the potential energy at the surface (Thomas, 1993), the effective acceleration, its angle to the surface normal (slope), and the dynamic height (Vanicek and Krakiwsky, 1986) which uses an area-averaged acceleration to scale the potential energy values. We tested several areas for the variations in slope and potential: the whole object, the darker part of the waist (Fig. 3), the whole mapped waist, and the entire 360° longitude range between 10°N and 60°N. For these different areas of the surface we find the area-averaged slopes, and the area-averaged variance of the potential, the latter scaled for the average potential because different densities impose different absolute potentials.

We made model predictions assuming primary rotation periods of 14, 16 and 18 h, and for bulk nuclear mean densities between 120 and 800 kg m^{-3}. The results for the 16-h period, likely the most relevant, are shown in Fig. 8. The results for an 18-h period give minima at slightly lower mean densities; the results for a 14-h period yield slightly higher mean densities. Results from calculation of average slope and variation of the potential energy (scaled for average values within an area) give similar, but not identical relations. Modeling the entire surface yields a distinct minimum for both average slope and potential variance (Table 2). These minima range from 265 kg m^{-3} to 300 kg m^{-3}. The waist region gives a minimum average slope at a density of 340 kg m^{-3}, but yields no minimum using potential variance. The dark portion of the waist provides no minimum for any period or measure. The difference in these results from those of Richardson and Bowling is chiefly in the area selected; results of whole-body measures in the two studies are essentially identical. Because these minima are judged significant based on process assumptions, we have no formal way of applying uncertainty ranges to these values in Fig. 8. From these plots alone we would infer a mean density between 265 and 340 kg m^{-3}.

Table 2
Densities for minima of variance of slopes and of potential.

Area	Density from slope (kg m^{-3})	Density from potential variance (kg m^{-3})
All	300	265
Waist	340	NM
Dark	NM	NM
Period = 16 h		
NM = no minimum		

5.2. Insights from topographic profiles

We attempt to refine the density inferences by reference to topographic profiles shown in Fig. 9. These show north–south profiles of dynamic heights at two longitudes for the 16-h rotation period. These profiles emphasize the variation of topography within the waist and the range of mean densities that come close to making part of the waist nearly flat, but which still leave noticeable slopes at other locales.

The simplest approach is to see what mean density gives the waist area (generally on these plots between *x*-axis values of 0.05 and 0.80 km) the flattest profiles; this value is ~230–240 kg m^{-3}. Values of 200–300 kg m^{-3} also appear consistent with a low, relatively flat waist region. These profiles also illustrate that global relief is minimal for densities near 250 kg m^{-3}.

Do the possible geological interpretations of the waist warrant matching an equipotential? This smooth surface might represent an equipotential surface, that is, it might be an area of ponding of loose material that cannot support slopes and is all close to the same potential. It might represent a relatively low area that is accumulating materials but has not entirely been flattened. It is bounded on the south by a transition to rougher terrain, sometimes gradually, at latitudes ranging from ~0 to ~30°N. The northern boundary is gradational over ~100 m at latitudes of ~56–60°N. The waist does not have a sharp boundary such as do "ponds" on Eros (Robinson et al., 2001) or the Muses Sea on Itokawa (Fujiwara et al., 2006). Although ponds are visibly distinct, there is a suggestion that some of the ponds on Eros are not completely "flat" (Roberts et al., 2012). The waist on Hartley 2 does not show flow fronts or other likely indicators of discrete flow units. Thus, while the images suggest low-slope processes, there is no clear geological restriction on how flat this region is.

The other darker smooth areas in the large lobe might be expected to either be flat, locally low, or perhaps show slopes indicative of a flow, especially for the elongate one at ~50°S, and 338–38°E (Fig. 3). These features occur in slightly lower regions than their surroundings, though the differences are largely <15 m. We note that the rotational light curves of H_2O and CO_2 (Besse et al., 2011) imply that the smaller lobe is much more active than the larger lobe so that transfer of material from the smaller lobe to these

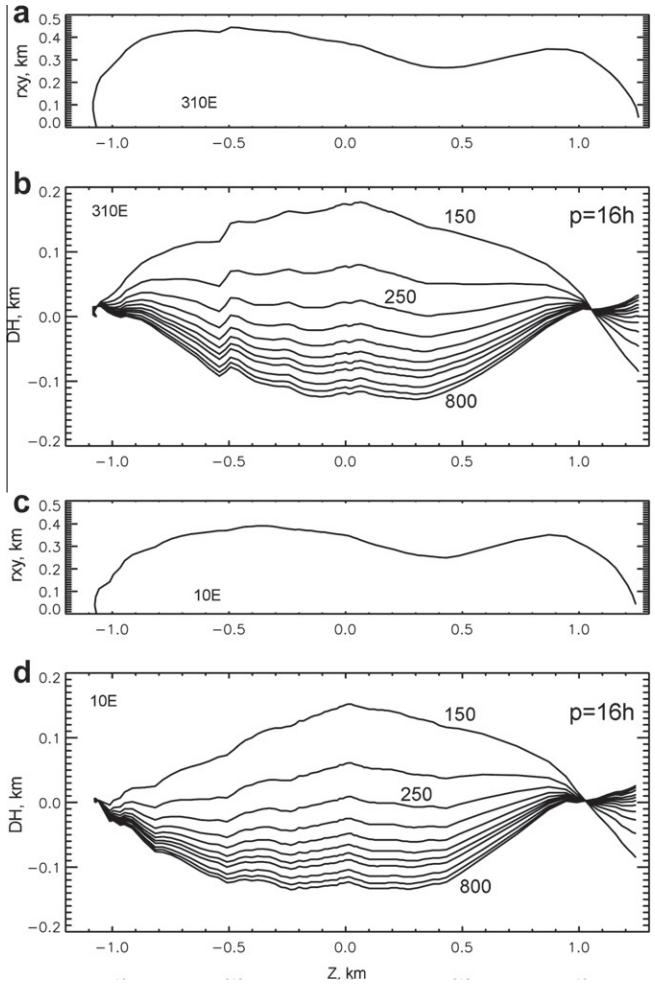

Fig. 9. Shape and dynamic heights along two longitudinal traverses. (A) 310°E, radius to surface. (B) Calculated topography along trace as a function of assumed mean density in kg m^{-3}, noted for three of the curves. Spin period of 16 h. (C) Same as (A) for 10°E. (D) Same as (B) for 10°E. The potential energies, or heights, are calculated relative to the south pole. Other points at the same rotational distance can all have the same rotational energy, which added to the same relative body mass potential results in curves recrossing at a point.

regions is plausible. Slopes within most dark areas exceed 5° no matter what the assumed density or rotation period.

5.3. Density summary

The model results in Fig. 8 and Table 2 suggest a mean density of 265–340 kg m^{-3}. The two sample profiles in Fig. 9 suggest a mean density between 200 and 300 kg m^{-3}. The limitations of our assumptions mean that systematic effects might allow a broader range of mean densities, probably on the higher side. We adopt a range of 200–400 kg m^{-3} (300 ± 100 kg m^{-3}) as approximate range using minimal significant figures. The upper value is not really constrained by Fig. 8; interpretation of Fig. 9 is the only upper bound possible with our approach, and we adopt 400 kg m^{-3} because of Fig. 8 results and the possible applicability of a still shorter rotation period. These results are broadly consistent with those of Richardson and Bowling (2012) who obtain 140–520 kg m^{-3}. The inferred density of Hartley 2 is within the range of estimates for Tempel 1 of 400 + 600/−200 kg m^{-3} (Richardson et al., 2007).

The density modeling uses only a homogeneous interior. If this is an assembly of two originally separate pieces, each might have a different mean density. Additionally, the deeper interior might have a different density from that of the surface regions. Investigation of these parameter spaces is left for later study. The simplicity of the current model emphasizes that the inferred density of 200–400 kg m^{-3} probably is an optimistic rendering of the uncertainty. By far our greatest concern with this modeling apart from assumptions of geologic processes, is that it is a static model of dynamic processes: the rotation and the surface accelerations have been changing, and the surface has been changing also. The observed shape is almost certainly an integrated effect of processes that has not reached, nor will it likely reach, an equilibrium form.

5.4. Meaning of a very low density

A density of 300 kg m^{-3} would require a high mean nucleus porosity, >70%, that could originate by inefficient packing of elongate or irregularly shaped particles and/or macroscopic voids. Particle densities would be roughly 930 kg m^{-3} for H_2O, 1500 kg m^{-3} for CO_2, ~800 kg m^{-3} for CO and 2500–3500 kg m^{-3} for refractory, rock-forming materials (e.g., silicates, metal sulfides, amorphous carbon). An upper limit of mean density of 520 kg m^{-3} would require ~45% porosity for water ice particles, and >50% for modestly more dense particles such as CO_2 ice or silicates. The ejection of loose clumps of material that rapidly disaggregate (A'Hearn et al., 2011) is consistent with a low-density assemblage. The different terrains on the surface indicate the operative processes sort materials and/or have different stages of development. The different relative amounts of CO_2 and H_2O (Besse et al., 2011; Feaga et al., 2011) also indicate either sorting of materials, global inhomogeneities, or different stages of processes in different regions of the comet nucleus.

6. Changing Hartley

6.1. Mass loss by Hartley 2

In order to estimate the total mass loss by Hartley 2 at a given apparition, we consider primarily the observations of the water release as determined from Ly-α measurements with the SWAN instrument on the Solar and Heliospheric Observatory (SOHO) (Combi et al., 2011a,b). These data cover the 1997 and 2010 apparitions and show clearly that the activity decreased by roughly a factor 3 from 1997 to 2010. The SNR is much better in 1997 so we use that apparition to integrate around the orbit.

In the 1997 apparition, the water production peaked at log(Q) = 28.55 molecules s^{-1} a few days after perihelion. We have carried out a numerical integration over the observed portion of the orbit using linear interpolation between each of the data points and we have also analytically integrated the power law obtained by assuming straight lines, eyeball fitted in log(Q) vs. log(Δt) (steeper before perihelion than after; Δt is time since perihelion). The two approaches agree within 20%. We have extended the range in heliocentric distance slightly using two points based on OH measurements supplied by Knight and Schleicher (2012) at 50 days pre-perihelion, log(Q) = 27.64 s^{-1}, and 66 days post-perihelion, log(Q) = 27.69 s^{-1}, both nearly an order of magnitude below the peak. To estimate the contribution further from perihelion, Meech et al. (2011) show from water-sublimation models, that the heliocentric light curve data (scattered light measurements from the dust) is consistent with the activity beginning ~450–500 days pre-perihelion near 4.3–4.2 AU. This is consistent with what was seen in previous apparitions by observers as compiled by Ferrin (2010). Post-perihelion activity continued through aphelion, turning off between 200 and 400 days post-perihelion (near r = 5.6 AU). Although Meech et al. (2011) suggest that this continued presence of grains in the coma is from CO_2 outgassing, we as-

sume here that the continuation through perihelion is due primarily to the rapidly increasing lifetime at large heliocentric distances of the icy grains that were released earlier and seen so prominently at this apparition (A'Hearn et al., 2011) and that the outgassing stops at 400 days. This yields a conservative lower limit on the total mass loss. If the average production rate during the decline to zero is as high as 10^{24} s^{-1}, roughly 1/3 the value suggested by the apparent magnitude at 250 days, it adds only about 2% at each end to the total mass loss. This computation yields a conservative lower limit of the total water release of 1.5×10^{35} molecules or 4.5×10^{12} g. From measurements during the flyby we know that CO_2 is about 30% by mass of H_2O. If we assume dust/gas = 1, the total mass loss during the 1997 apparition was 1.2×10^{13} g. During the 2010 apparition, therefore, it was roughly 4×10^{12} g. These numbers are very sensitive to the dust/gas ratio, a poorly determined parameter for all comets (due to the mass of dust being dominated by the largest grains in many comets), but half this value (the ices) is a solid lower limit and the value could range up to 2 or 3 times larger than the value above.

Using the surface area from Table 1, the mass loss in 1997 corresponds to ~2300 kg m^{-2}. For a bulk density of 300 kg m^{-3}, this value corresponds to a loss of 7.7 m of material everywhere on the surface. In terms of the upper range of the density from Richardson and Bowling (2012) (and a more typical density for other, better determined nuclei) a mean density of 520 kg m^{-3} would suggest loss of 4.4 m per orbit. Using the volume from Table 1, and a density of 300 kg m^{-3}, the mass loss during the 1997 apparition was roughly 5% of the total mass of the nucleus and thus about 2% of the total mass during the 2010 apparition. An upper density value of 520 kg m^{-3} would suggest a loss nearer 3% of the nuclear mass in 1997 and 1% in 2010. Even allowing for a factor of a few uncertainty due to the unknown dust/gas mass ratio, this mass loss, both as an average depth and as a fraction of the mass of the nucleus, is far higher than that found for the much larger nucleus of 9P/Tempel 1 (~1/3 m/orbit or ~3×10^{-4} mass/orbit; Thomas et al., 2012).

The above calculations are average amounts over the entire surface. However, all the evidence from the flyby (A'Hearn et al., 2011) suggests that much of the material is lost from sub-surface outflows that are localized, so collapse features might be the expected expression one would see in images from different apparitions, perhaps analogous to those seen near the smooth flow on 9P/Tempel 1 (Schultz et al., 2011). However, collapse forms are not obvious in the images. Perhaps some of the dark areas might be termed sags (Section 5.2) related to loss of material from extended sub-surface regions.

6.2. How is the surface shaped?

The somewhat more elongated average shape of cometary nuclei compared to small asteroids has been attributed to effects of surface mass loss by sublimation (Jewitt et al., 2003). In detail, however, sublimation lowering of surfaces generates positive feedback effects (such as formation on Earth of suncups, penitents, or inverted topography; Lliboutry (1954), and discussed in the case of comet nuclei by Malin and Zimbelman (1986) that leave a rough and variegated surface quite unlike what is visible on Hartley 2. Our close-up views of comets are limited and in situ observations nonexistent, so we must consider general principles and make the best available comparisons to infer how this object evolves.

The bi-lobed shape suggests possible formation from two pieces. The near axial symmetry suggests effects related to spin and gravity rather than to random events such as impact cratering. As noted above this comet does not display the erosional and depositional forms found on Tempel 1 (and likely on Wild 2 and Borrelly; Soderblom et al., 2002; Brownlee et al., 2004) that contribute to a complicated shape that is not symmetric and which has considerable topography relative to gravity. Indeed, even though dispersal of material in jets, carrying particles that continue to fragment (A'Hearn et al., 2011) is obvious, the vent geometry, if there are discrete vents, is elusive, and any flow forms likely vastly different from those on Tempel 1 (Belton and Melosh, 2009). There are some areas, the darker patches (Section 4.3) that suggest deposition, but which are not gravitationally confined materials such as the "ponds" on Eros, because they have some gravitational slopes. Even the waist area has roughness on the scale of meters vertically and regional slopes of a few degrees for any mean density, and thus is also not a simple deposit, even though its shape strongly suggests some mechanism of regional smoothing. Thus we must look for more indirect routes of molding the surface of this comet.

As noted in Section 6.1 the mass flux from this comet could amount to several meters of surface lowering per orbit, and given the distributed jets and lack of large vent morphology, the possibility arises of subsurface cavities supplying material and then being subject to collapse. The size and depth of such cavities would presumably not greatly exceed an orbital skin depth, thus would need to be numerous, nearly ubiquitous, and only marginally resolvable. At 7 m/pixel the surface shows no indication of dominance of collapse morphology. A trough <15 m deep exists at high southern latitudes (Fig. 1 bottom lit area; Fig. 7 near bottom), but much of this topography may be constructional clustering of the bright knobs. More intriguing are the smooth, slightly sloping, darker areas that appear to be either parts of bowls or of tilted segments, albeit near the limits of our measurement precision (Fig. 7). These depressions might be remnants of collapse of connected large voids partially filled and smoothed by material formerly above the voids ("crust") or partially covered by some materials mobilized near the surface by other vents.

The presence of mounds may suggest eruptive and constructive mechanisms at work, and the ejection of particles that subsequently supply much of the mass loss by sublimation (A'Hearn et al., 2011; Harmon et al., 2011; Kelley et al., 2012) indicates an environment rich with material that could form brighter local deposits. There is the possibility that the average surface is losing material while some of the mounds undergo deposition and upward growth. The height of the mounds (generally <30 m; Section 4.1) might be the net result of loss and growth before the mounds collapse. This height might reflect the strength of the mounds, which can be crudely estimated based on ρgh, where $\rho = 300$ kg m^{-3}, $g = 4 \times 10^{-5}$ ms^{-2}, and $h = 3 \times 10$ m, assuming a density at the low end of our mean values. This approximation gives a value of 0.4 Pa. Such a weak material would be consistent with local accumulation of what might be close to snowflakes. Given the small relief elsewhere on the comet nucleus, strengths estimated using these assumptions for materials anywhere on this object will be very low.

The high rate of mass ejection does suggest there should be some small, low-velocity fraction that may not initially escape. This material might be distributed widely over the nucleus, and could possibly flow with the tenuous gasses evolving from ice particles into the gravitationally lower regions. Such material would have essentially zero strength and be consistent with minimal topography on a very low-gravity object.

7. Summary

Hartley 2 is distinguished by a nearly axially symmetric, bilobed shape. An extremely active comet partly by virtue of expelling solid water–ice particles, its surface may suffer average loss of a few meters per orbit. Its surface features, chiefly mounds <30 m in dimension, relatively darker smooth areas, and a waist

with local topography <2 m do not easily compare to obvious erosional and depositional forms such as the pits and smooth deposits on Tempel 1. The smooth shape, and especially the waist, suggest processes whose net effects reduce topography on horizontal scales of >100 m. The shape combined with assumptions of smoothing processes suggests a mean density of 200–400 kg m^{-3}. This mean density implies loss of >1% of the nuclear mass per orbit. The axial near symmetry suggests no significant role for random events such as craters but does suggest interacting roles for insolation, spin, and gravity.

Acknowledgments

Most of the work for this paper was funded by NASA, through Contract NNM07AA99C to the University of Maryland from NASA's Discovery and New Frontiers Program Office. Part of this research was carried out at the Jet Propulsion Laboratory, California Institute of Technology, under a contract with the National Aeronautics and Space Administration. Technical assistance provided by A. Quick, K. Consroe, R. Rich Goldweber, and C. Jackman. Two reviewers helped find mistakes and improve the presentation.

References

A'Hearn, M.F. et al., 2005a. Deep Impact: Excavating Comet Tempel 1. Science 310, 258–264.
A'Hearn, M.F., Belton, M.J.S., Delamere, A., Blume, W.H., 2005b. Deep Impact: A large-scale active experiment on a cometary nucleus. Space Sci. Rev. 117, 1–21.
A'Hearn, M.F. et al., 2011. EPOXI at Comet Hartley 2. Science 332, 1396–1400.
Belton, M.J.S., Melosh, J., 2009. Fluidization and multiphase transport of particulate cometary material as an explanation of the smooth terrains and repetitive outbursts on 9P/Tempel 1. Icarus 200, 280–291.
Belton, M.J.S. et al., 2012. The complex spin state of 103P/Hartley 2. Kinematics and orientation in space. Icarus 222, 595–609.
Besse, S. et al., 2011. Temporal and compositional variation of jets activity in Comet Hartley 2 as observed by Deep Impact. EPSC-DPS Joint Meeting 197.
Brownlee, D.E. et al., 2004. Surface of young Jupiter Family Comet 81 P/Wild 2: View from the Stardust spacecraft. Science 304, 1764–1769.
Combi, M.R., Lee, Y., Patel, T.S., Mäkinen, J.T.T., Bertaux, J.-L., Quemerais, E., 2011a. SOHO/SWAN observations of short-period spacecraft target comets. Astron. J. 141, 128 (13pp.).
Combi, M.R., Bertaux, J.-L., Quemerais, E., Ferron, S., Mäkinen, J.T.T., 2011b. Secular light curve of Comet 103P/Hartley 2, target of the EPOXI mission. Astrophys. J. 734, L6 (5pp.).
Dermott, S.F., Thomas, P.C., 1988. The shape and internal structure of Mimas. Icarus 73, 25–65.
Feaga, L.M. et al., 2011. Heterogeneity of Comet 103P/Hartley 2's Gaseous Coma. Lunar Planet. Sci. 42, 2461 (abstract).
Ferrin, I., 2010. Secular light curve of Comet 103P/Hartley 2, target of the EPOXI mission. Planet. Space Sci. 58, 1868–1879.
Fujiwara, A. et al., 2006. The rubble-pile Asteroid Itokawa as observed by Hayabusa. Science 312, 1330–1334.
Groussin, O., Lamy, P., Jorda, L., Toth, I., 2004. The nuclei of Comets 126P/IRAS and 103P/Hartley 2. Astron. Astrophys. 419, 375–383.
Hampton, D.L. et al., 2005. An overview of the instrument suite for the Deep Impact mission. Space Sci. Rev. 117, 43–93.
Harmon, J.K. et al., 2011. Radar observations of Comet 103P/Hartley 2. Astrophys. J. Lett. 734, L2 (4pp.).
Jewitt, D., Sheppard, S., Fernandez, Y., 2003. 143P/Kowal–Mrkos and the shapes of cometary nuclei. Astron. J. 125, 3366–3377.
Kelley, M.S. et al., 2012. A distribution of large particles in the coma of Comet 103P/Hartley 2. Icarus, submitted for publication.
Klaasen, K.P. et al., 2008. Invited article: Deep Impact instrument calibration. Rev. Sci. Instrum. 79, 091301 (77pp.).
Knight, M.M., Schleicher, D.G., 2012. The highly unusual outgassing of Comet 103P/Hartley 2 from narrowband photometry and imaging of the coma. Icarus, submitted for publication.
Li, J.-Y. et al., 2012. Photometry of the nucleus of comet 103P/Hartley 2. Icarus, submitted for publication.
Lindler, D., A'Hearn, M.F., Besse, S., Klaasen, K., 2012 Interpretation of results of deconvolved images from the Deep Impact spacecraft High Resolution Instrument. Icarus, submitted for publication.
Lisse, C.M. et al., 2009. Spitzer Space Telescope observations of the nucleus of Comet 103P/Hartley 2. Publ. Astron. Soc. Pacific 121, 968–975.
Lliboutry, L., 1954. The origin of penitentes. J. Glaciol. 2 (15), 331–338.
Malin, M.C., Zimbelman, J.R., 1986. Surface morphology of cometary nuclei. Lunar Planet. Sci. 17, 512–513 (abstract).
Meech, K.J. et al., 2011. EPOXI: Comet 103P/Hartley 2 observations from a worldwide campaign. Astrophys. J. 734, L1 (9pp.).
Richardson, J.E., Bowling, T.J., 2012. The combined effect of gravity and rotation on small-body surface terrains: Gleaning body density from spin, shape, and slopes. Icarus, submitted for publication.
Richardson, J.E., Melosh, H.J., Lisse, C.M., Carcich, B., 2007. A ballistics analysis of the Deep Impact ejecta plume: Determining Comet Tempel 1's gravity, mass, and density. Icarus 190, 357–390.
Roberts, J.H., Barnouin, J.S., Prockter, L.M., Kahn, E.G., Gaskell, R.W., 2012. Not all ponds are flat: A stereo phoclinometric analysis of Eros topography. Lunar Planet. Sci. 46. Abstract #2450.
Robinson, M.S., Thomas, P.C., Veverka, J., Murchie, S., Carcich, B., 2001. The nature of ponded deposits on Eros. Nature 413, 396–400.
Schultz, P.H. et al., 2011. Geology of 103P/Hartley 2 and nature of source regions for jet-like outflows. Lunar Planet. Sci. 42. Abstract 2382.
Semenov, B.V., Acton, C.H., 2006. Deep Impact SPICE KERNELS. V1.0, DI-C-SPICE-6-V1.0, NASA Planetary Data System.
Semenov, B.V., Elson, L.S., Acton, C.H., 2004. Stardust SPICE KERNELS. V1.0, SDU-C-SPICE-6-V1.0, NASA Planetary Data System.
Soderblom, L. et al., 2002. Observations of Comet 19P/Borrelly by the miniature integrated camera and spectrometer aboard deep space 1. Science 296, 1087–1091.
Sunshine, J.M. et al. 2011. Water ice on Comet 103P/Hartley 2. EPSC-DPS Joint Meeting, 1345.
Syal, M.B., Schultz, P.H., Farnham, T.L., A'Hearn, M.A., Dearborn, D.S.P., 2012. Jet formation on comet Hartley 2. Icarus, submitted for publication.
Thomas, P.C., 1989. The shapes of small satellites. Icarus 77, 248–274.
Thomas, P., 1993. Gravity, tides, and topography on small satellites and asteroids. Icarus 105, 326–344.
Thomas, P.C. et al., 2002. Eros: Shape, topography, and slope processes. Icarus 155, 18–37.
Thomas, P.C. et al. 2012. The nucleus of comet 9P/Tempel 1: Shape and geology from two flybys. Icarus 222, 453–466.
Vanicek, P., Krakiwsky, E.J., 1986. Geodesy: The Concepts, second ed. Elsevier, New York, 697pp.